

Stoichiometry and Orientation- and Shape-Mediated Switching Field Enhancement of the Heating Properties of Fe_3O_4 Circular Nanodiscs

Gopal Niraula^{1,2}, Jose A. H. Coaquira², Fermín H. Aragón², Andris F. Bakuzis,⁴ Bianca M. G. Villar⁵, Flavio Garcia⁵, Diego Muraca⁶, Giorgio Zoppellaro⁷, Ahmad I. Ayesh^{8,9}, and Surender K. Sharma^{1,10,*}

¹Department of Physics, Federal University of Maranhão, São Luis, Brazil

²Laboratory of Magnetic Materials, NFA, Institute of Physics, University of Brasília, Brasília, Brazil

³Laboratory of Thin Films, School of Physics, National University of Saint Augustine, Arequipa 001, Peru

⁴Institute of Physics, Federal University of Goiás, 74690-900, Goiânia, GO, Brazil

⁵Brazilian Center for Research in Physics - CBPF, Rio de Janeiro, RJ, Brazil

⁶Institute of Physics “Gleb Wataghin” (IFGW), University of Campinas, Campinas, Brazil

⁷Regional Centre of Advanced Technologies and Materials, Faculty of Science, Palacky University in Olomouc, Slechtitelu 11, 78371 Olomouc, Czech Republic

⁸Center for Sustainable Development, Qatar University, P. O. Box 2713, Doha, Qatar

⁹Department of Mathematics, Statistics and Physics, Qatar University, P. O. Box 2713, Doha, Qatar

¹⁰Department of Physics, Central University of Punjab, Bathinda, India



(Received 9 July 2020; revised 6 November 2020; accepted 14 December 2020; published 28 January 2021)

The generation of topological magnetic vortex-domain structures in iron-oxide nanomaterials has promising applications in biomedical scenarios, such as heat generators for hyperthermia treatments. In this report we describe alternative kinds of magnetic-vortex nanoparticles, circular Fe_3O_4 nanodiscs (NDs), and dissect their heating properties by in-depth investigation of their shape and size, stoichiometry, orientations, and switching field “ H_S ” behaviors, through experiments and theoretical simulation. We find that the stoichiometric NDs show better heating performance than nonstoichiometric materials because of the significant electron hopping between Fe^{3+} and Fe^{2+} ion. The higher heating efficiency (in terms of specific absorption rate, SAR) is observed only for the higher switching field regime, an effect that is associated with the parallel and perpendicular alignment of nanodiscs with respect to low and high ac magnetic field, respectively. A higher SAR of approximately 270 W/g is observed at a higher switching field (approximately 700 Oe) for NDs of diameter 770 nm, which increases by a factor of 4 at a switching field of approximately 360 Oe for NDs of diameter 200 nm. The reported results suggest that the heating efficiency in these systems can be enhanced by controlling the switching field, which is, in turn, tuned by size, shape, and orientation of circular magnetic vortex nanodiscs.

DOI: 10.1103/PhysRevApplied.15.014056

I. INTRODUCTION

The technological application of magnetic-oxide-based nanoparticles (NPs), such as magnetite (Fe_3O_4) and maghemite ($\gamma\text{Fe}_2\text{O}_3$) nanosystems, have been intensively researched and screened over the last three decades in biomedical domains, especially for their use in magnetic resonance imaging (MRI), as drug-delivery systems and in magnetic fluid hyperthermia (MFH) treatments [1–5]. Fe_3O_4 and $\gamma\text{Fe}_2\text{O}_3$ nanoparticles express high biocompatibility under physiological conditions and are efficient magnetic nanoheaters. The heating efficiency of magnetic nanoparticles (MNPs) is therefore regarded by many

researchers in the biomedical field as a promising therapeutic tool for enhancing selectivity in thermal therapies [6–8]. The technique involves the use of MNPs intravenously administered that are subsequently subjected to an external ac magnetic field at a defined frequency; in this way, it can be generated local heat to those tissues in which NPs are mostly localized; in principle, this procedure allows specific tumor locations to be targeted and heat only to be delivered in the tumor area without affecting the healthy tissues [9,10]. Experimental work with superparamagnetic Fe_3O_4 NPs showed, however, that the induced heat diminishes due to low saturation magnetization (M_S) and coercivity (H_C), and hence large quantities of NPs need to be injected to obtain a therapeutic effect, which in turn might enhance the toxicity [11]. To tackle

*surender76@gmail.com

this issue, several works have been optimized; which include replacing iron oxide by others with higher M_S (Fe, FeCo etc.); tuning the size of the nanoparticles; enhancing the H_C (or anisotropy) through exchange coupling and doping [12–15], or modifying the morphology (aspect ratio, shapes): cubes, octopods, octahedral, cube octahedral of the MNPs [3,9,16–20], to tune their anisotropy and improve their overall heating efficiency. Ferro- and ferrimagnetic (FM and FIM) iron-oxide NPs with multidomain structure exhibit better heating performance as compared with superparamagnetic Fe_3O_4 . Nonetheless, proclivity to agglomeration of FM and FIM NPs remains a major challenge to overcome the preparation of stable colloidal suspension [3,21,22]. Recently, it has been shown that such limitations can be addressed by tailoring NP geometry, such as nanodiscs (NDs), nanorings (NRs) etc. [3,4,18,23–26]. The disc-shaped MNPs have high M_S , large surface energy, which increase their effective anisotropy, and at bigger sizes, they develop a vortex magnetic domain structure (with negligible H_C and M_R) that ensure null magnetization in the absence of magnetic field, hence reducing the long-range dipole-dipole interactions and avoiding the unwanted particle agglomeration. The nucleation (H_n) and annihilation field (H_{an}), also called switching field (H_S), are responsible for the nucleation and annihilation of a different state in the NPs.

An efficient magnetohyperthermia property has been reported in the literature in the permalloy ($\text{Fe}_{20}\text{Ni}_{80}$) nano- and microdiscs (NDs and MDs) [24,27]. Recently, another work describing orientation-mediated heating performance of magnetic vortex in Fe_3O_4 NDs has also been investigated, which exhibited the highest specific absorption rate (SAR) reported so far in the literature [3]. Nevertheless, there is still a lack of critical understanding of the geometrical variables connected to the observed switching field distribution as a function of different shape, size, and orientation of NDs. Understanding the physical principles underneath such geometry-based switching field “ H_S ” and their macroscopic effects on heating properties may lead to the desired generation of nanomagnetic systems in which the heating efficiency is achieved fully in a controlled way. In this work we describe a systematic study of microwave-assisted hydrothermal (MAH) synthesis of Fe_3O_4 NDs (stoichiometric and nonstoichiometric) and analyze the systems’ magnetic heating performances as a function of stoichiometry, geometrical factors, and orientation- and shape-mediated switching fields. We employ the MAH route for the material’s assembly because it is fast and an energy-efficient synthetic approach [28–30].

II. EXPERIMENTAL SECTION

A. Synthesis of $\alpha\text{Fe}_2\text{O}_3$ and Fe_3O_4 nanodiscs

Two $\alpha\text{-Fe}_2\text{O}_3$ NDs are prepared by a MAH reaction of iron chloride (FeCl_3) with addition of sodium phosphate

(NaH_2PO_4) and sodium sulfate (Na_2SO_4) as additives at temperatures 200 and 220 °C. These NDs prepared at 200 and 220 °C give a nonstoichiometric disc (NSD) and a stoichiometric disc (SD), respectively. In brief, 0.06 mol l⁻¹ of FeCl_3 with 35 ml of distilled water are stirred for 15–20 min. The additives NaH_2PO_4 (4.32×10^{-3} mol l⁻¹), and $\text{Na}_2\text{SO}_4 \cdot 10\text{H}_2\text{O}$ (1.65×10^{-3} mol l⁻¹) mixed with 3 ml of distilled water separately and finally mixed with FeCl_3 solution to make a mixture of final volume 38 ml. After vigorous stirring for 10 min, the mixture is transferred into a reaction vessel in a Synth’s microwave reactor, with an output power of 1000 W. The working cycle of the microwave reactor is set as 20 °C/min of rapid heating until 200 and 220 °C from room temperature for 60 min. The system is then allowed to cool down to room temperature, and the final material is centrifuged and washed with excess of distilled water and absolute ethanol and dried in a vacuum oven at 50 °C.

In this way, we obtain about 300 mg of $\alpha\text{Fe}_2\text{O}_3$ NDs, which is approximately 80% of FeCl_3 . Fe_3O_4 NDs are obtained via a reduction process with the corresponding $\alpha\text{Fe}_2\text{O}_3$ as the starting NDs. The dried $\alpha\text{Fe}_2\text{O}_3$ powders are annealed in a furnace at 550 °C under a continuous hydrogen-argon gas flow [$\text{H}_2/(\text{H}_2 + \text{Ar}) = 4/100$] for 6 h. The furnace is allowed to cool to room temperature while still under a continuous H_2 gas flow. As compared with the starting materials of $\alpha\text{Fe}_2\text{O}_3$, the size, shape, and morphology of Fe_3O_4 nanostructures are perfectly preserved in the reduction process.

B. Characterization

1. X-ray diffraction

A commercial x-ray diffractometer (Bruker, model D8 Advance) equipped with Cu K_α radiation is used to assess the crystal structure, in the 2θ range of 15° to 85°. The XRD patterns are analyzed with the Rietveld refinement method using General Structure Analysis System (GSAS) software within the EXPGUI Interface.

2. Electron microscopy

The morphology of the samples is investigated by using a JEOL 7100FT field-emission scanning electron microscope (FESEM, 1.2 nm resolution, operated at 10–30 kV) available at LABNANO/CBPF. The HRTEM is performed on a JEOL 2100F instrument using an accelerating voltage of 200 kV.

Fourier transform infrared spectroscopy: FTIR spectrometer (Bruker, model Tensor 27), equipped with attenuated total reflectance (ATR) accessory, is used to identify functional groups present in the nanoparticles.

3. Mössbauer spectroscopy

The measurements of ^{57}Fe Mössbauer spectra are performed in the transmission geometry using a constant

acceleration-type spectrometer with a ^{57}Co in Rh source kept at room temperature. The spectra are fitted by Normas and MosWin4.0.

4. Magnetometry

Next, dc magnetization (hysteresis) measurements are carried out in a vibrating sample magnetometer superconducting quantum interference device (VSM SQUID) (MPMS Quantum Design) equipped with a superconducting coil that produces magnetic fields up to ± 70 kOe at working temperatures from 5 and 300 K and zero-field-cooled (ZFC) and field-cooled (FC) measurements are performed in the temperature range of 5 to 350 K with applying 50 Oe field.

5. Micromagnetic modeling

Micromagnetic simulations are performed using the Mumax3.9 package. The magnetic parameters of Fe_3O_4 used in the micromagnetic simulation are listed as follows: saturation magnetization $M_S = 480$ emu/cc, exchange stiffness constant $A = 1.2 \times 10^{-6}$ erg/cm, magnetocrystalline anisotropy constant $K_1 = -1.35 \times 10^5$ erg/cc, $K_2 = -0.44 \times 10^5$ erg/cc [25]. The lateral cell size is $5 \times 5 \times 5$ nm 3 ; this lateral size (5 nm) is smaller than the exchange length (approximately equal to 10.7 nm) as defined by $L_{\text{ex}} = (2A/\mu_0 M_S^2)^{0.5}$ to assure the accuracy of simulation [31]. The Gilbert damping coefficient α is used as 0.5.

6. Construction of phase diagram

We start investigating the lower-energy configurations in the case of nanodiscs of thickness “ t ” and diameter “ d .” In the case, three idealized characteristic configurations are evaluated: (i) a single domain in plane (planar); (ii) single domain out of plane (perpendicular); (iii) a vortex state in which most of the magnetic moments lie parallel to the plane of the nanodiscs. The system relaxed to a local energy minimum, studied the final spin configuration and the lower-energy states in nanodiscs. Thereafter, we compare the energy of each final configuration, and select as a ground state with a lower-energy value. This process is

repeated for several diameter and thickness combinations and the phase diagrams are constructed as a function of the thickness “ t ” and diameter “ d .”

7. Magnetic hyperthermia

Magnetic hyperthermia is performed using the magneTherm system from nanoTherics. In order to estimate the heating efficiency of the nanoparticles, we use the standard hyperthermia calorimetric experiments. In these experiments, a vial with the sample is placed into a coil connected to a power generator, which allows us to control the amplitude of the ac field inside the coil. While the field is applied, a fiber optic temperature sensor inserted into the vial with the solution records the increase in temperature, and from the initial slope of these temperature versus time curves, one can obtain the SAR values:

$$\text{SAR} = C \frac{M}{m_{\text{MNP}}} \frac{dT}{dt},$$

where C is the specific heat capacity of the medium, M is the mass of the fluid, and m_{MNP} is the mass of the nanoparticles.

III. RESULTS AND DISCUSSION

As shown schematically in Fig. 1, the first step in the material synthesis involves assembly of the hematite ($\alpha\text{Fe}_2\text{O}_3$) nanodiscs, which are later reduced to Fe_3O_4 in the presence of Ar and H₂. Controlling the conversion of $\alpha\text{Fe}_2\text{O}_3$ NDs to Fe_3O_4 is a challenging task because it depends on several physiochemical factors, such as the concentration of Fe³⁺, annealing temperatures, time, gas-flow rate, concentration of H₂ gas, and amount of phosphate anions. Uncontrolled combination of H₂ and monobasic phosphate anions lead towards biphasic material; the high temperature and long duration for thermal reduction may provoke the shape coalescence [32,33]. In the literature, some thermal reductions are performed using a mixture of trioctylamine (TOA) and oleic acid (OA) in order to avoid coalescence of bare NPs [3]. However, as described in detail in the synthesis, we can maintain the

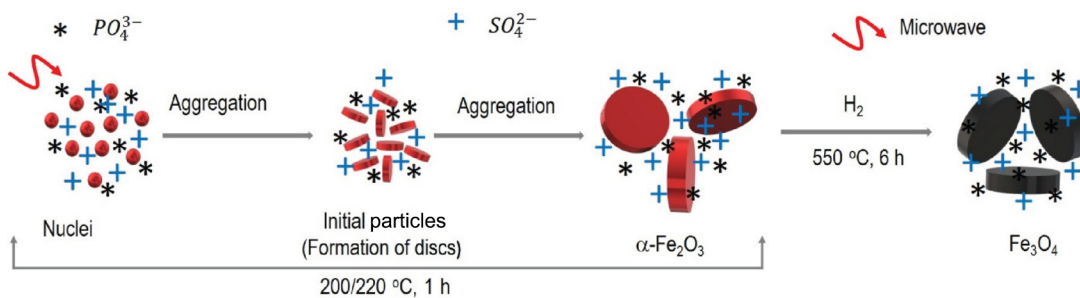


FIG. 1. Schematic illustration of the formation of Fe_3O_4 nanodiscs.

ND size, phase, and morphology without any addition of surfactants during the thermal reduction process.

Figure 2(a) shows the XRD pattern of the so-formed Fe_3O_4 nanodiscs along with their Rietveld analysis. All the diffraction peaks are readily indexed to a cubic spinel phase (space group: $Fd\text{-}3m$) with JCPDS No. 19-0629, $a = b = c = 8.37 \text{ \AA}$). No other scattering signals are observed that are addressable to impurities, such as $\alpha\text{Fe}_2\text{O}_3$, and $\gamma\text{Fe}_2\text{O}_3$, an indication for the presence of pure Fe_3O_4 phase in our NSD and SD samples. Figures 2(b) and 2(c) show the FESEM images of Fe_3O_4 NSD and SD. These materials exhibit average thickness (t) approximately 100 nm and a mean diameter (d) approximately 745 nm for NSD and approximately 770 nm for SD with aspect ratio ($\beta = t/d \sim 0.13$). The size of SD and NSD is similar since the initial size and morphology are preserved after reduction. The corresponding size distribution of $\alpha\text{Fe}_2\text{O}_3$ and Fe_3O_4 SD and NSD is given in Fig. S2 within the Supplemental Material [34]. HRTEM images reveal a lattice spacing of 0.254 and 0.198 nm for NSD, which corresponds to the lattice spacing of (311) and (400), whereas 0.253 and 0.197 nm for SD agrees well with (311) and (400) planes of inverse spinel Fe_3O_4 [35] [see Figs. 2(d) and 2(e)]. Polycrystalline structures are observed in both samples, NSD and SD, as analyzed through FFT pattern [inset of Figs. 2(d) and 2(e)].

The dc magnetization experiments, performed at 300 K, show saturation magnetization M_S for SD and NSD of approximately 83 emu/g and approximately 80 emu/g, respectively, shown in Fig. 3(a). The higher “ M_S ” of SD can be ascribed due its stoichiometry properties [36]. A small difference in “ M_S ” in both samples as compared with the bulk magnetite is probably due to the presence of cation vacancies and defects, and stoichiometry deviation

[36], which is subsequently discussed in Sec. 3. The low value of the coercive field (H_C) is observed in these materials, approximately 232 Oe and approximately 182 Oe for the SD and NSD, respectively. Although, the morphology of SD and NSD is somewhat similar, the higher “ H_C ” value for SD may point towards the existence of enhanced surface anisotropy, the contribution to that may arise from structural defects, broken symmetry bonds, and surface-strain effects [37].

There is always an open space for defects namely point defects, dislocations, stacking faults, subgrain boundaries, inclusions, and voids in the nanoparticles generated during the synthesis [38–40]. Generally, these defects can affect magnetization in two ways: (i) they can act as centers for the nucleation of new domain walls and aid magnetization reversal. This occurs at sites where the domain-wall energy is locally changed by physical or chemical defects, which would decrease magnetocrystalline anisotropy by creating a nucleation site and hence result in a decrease of H_C , (ii) the existence of domain walls on the surface and their movement can easily be blocked by the adsorbed phosphate layers, resulting in domain-wall pinning, which contributes to effective anisotropy, which increases H_C in SD. It is worthwhile to mention that it is difficult to determine the types of defects and the way in which they affect the magnetization, but their influence on H_C is easily understood by analyzing the effective anisotropy (i.e., magnetocrystalline anisotropy, and surface anisotropy) [41]. In the present study, the surface anisotropy might have the contribution of defects; however, it is still hard to discern the exact mechanism. The observed surface anisotropy contribution is estimated as $3.02 \times 10^6 \text{ erg/cc}$ (for NSD) and as $3.35 \times 10^6 \text{ erg/cc}$ (for SD). These values are calculated using the law of approach to saturation (Appendix)

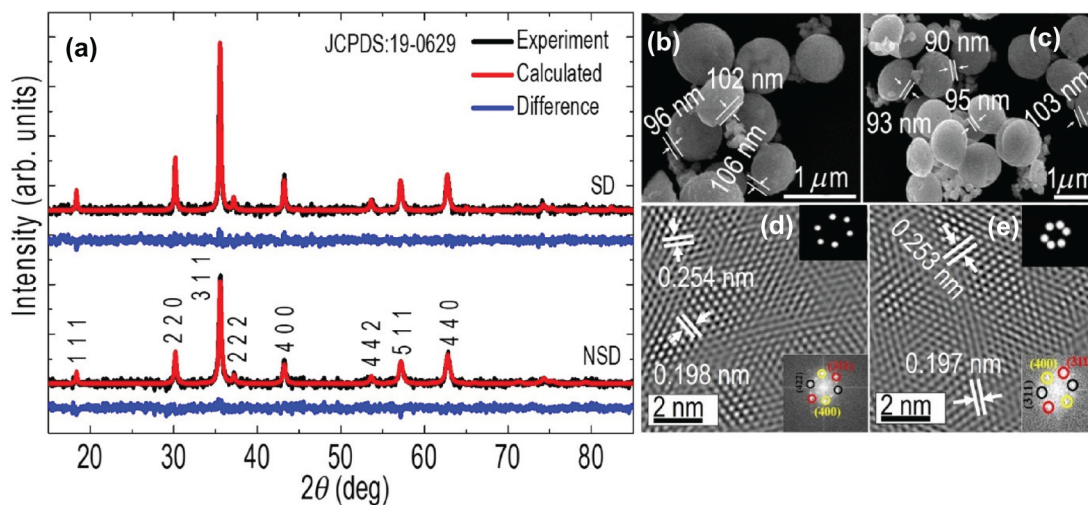


FIG. 2. (a) XRD with Rietveld analysis, (b) and (c) are FESEM images after reduction, and (d) and (e) are HRTEM images of NSD and SD, respectively. Upper insets of (b) and (c) are magnified images with the same scale. Upper and lower insets of (d) and (e) are IFFT and FFT images.

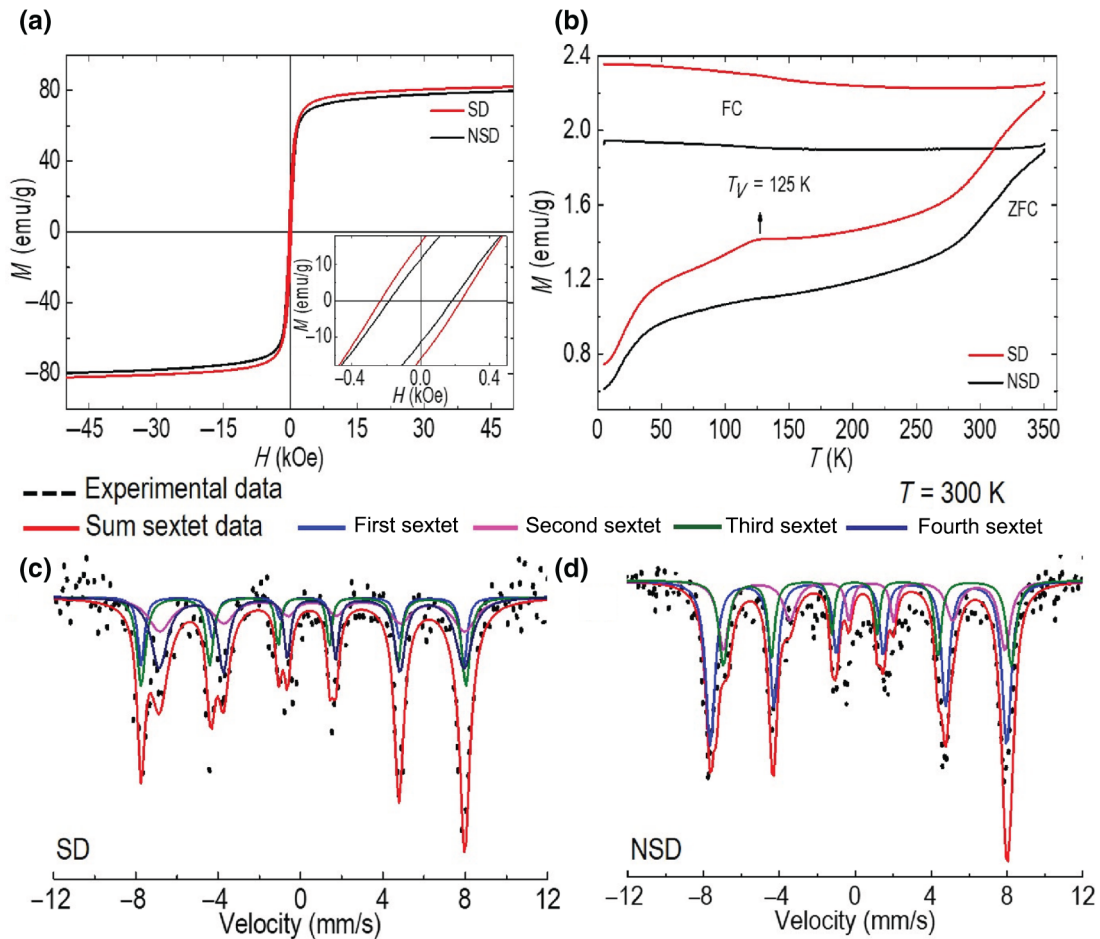


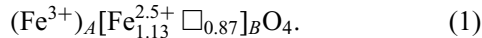
FIG. 3. (a) The hysteresis loop recorded at 300 K, (b) ZFC FC measurement, and (c) and (d) Mössbauer spectra of SD and NSD, respectively, at $T = 300$ K.

[42], which is one order of magnitude larger than for bulk Fe_3O_4 (1.1×10^5 erg/cc) [9].

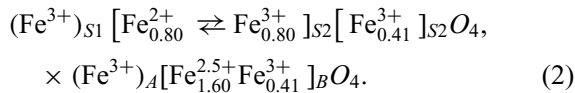
The zero-field-cooling and field-cooling (ZFC FC) curves exhibit a prominent Verwey transition (“ T_V ”) for the SD at approximately 125 K, which is a typical characteristic of stoichiometric Fe_3O_4 , whereas no such transition is observed for the NSD, which is clearly seen in Fig. 3(b). The “ T_V ” for bulk Fe_3O_4 , is $T_V \approx 119$ K [43]. The term “ T_V ” depends on the stoichiometry of Fe_3O_4 and is very sensitive to the composition of NPs as well as on the growth mechanism [44,45]. The room-temperature Mössbauer-spectroscopy analysis for both nanodiscs is well fitted considering sextet patterns (magnetic subspectra). From Fig. 3(c), the spectrum for SD is well resolved by four sextets. The hyperfine parameters for both samples, Fig. S4 within the Supplemental Material [34] are consistent with the two crystallographic sites of iron cations in the cubic spinel ($Fd\text{-}3m$) structure of Fe_3O_4 [35]. However, the spectral area ratio on Fe cations residing on A and B sites diverge from those present in the bulk magnetite (i.e., 1:2 for free-defect crystals) and is 1:1.38. Such

a divergent A/B ratio of the Fe population is evident for the samples that are not perfectly stoichiometric. These results can be interpreted by considering the existence of a core-shell structure as the model system, assuming that the core region follows the bulk Fe_3O_4 composition, i.e., stoichiometric, while the shell region is nonstoichiometric, due to vacancies and defects. In Fig. 3(c), two sextets, blue and pink line, are fitted using bulk parameters. These signatures belong to the Fe residing in the core region. From the fitting analysis we obtain Fe cations with 12 and 24% residing in A and B sites, respectively, thus 36% population of Fe is stoichiometric Fe_3O_4 . In this region of SD, charge ordering between Fe^{3+} and Fe^{2+} must occur, such as electron hopping ($\text{Fe}^{2+} \rightleftharpoons \text{Fe}^{3+}$) at the octahedral sites, a factor that has a major contribution in tuning the transition temperature as observed in ZFC magnetization data. Similarly, the other two sextets considered for the shell region, drawn in Fig. 3(c) with the navy line and the green line, represent the Fe residing in the A site and the B site, and their ratio is consistent with nonstoichiometric NPs. The population ratio in the A site and the B site is, in

fact, 1:1.13 and such a value indicates the presence of cation vacancy and defects. In the case of cation vacancies in the *B* site, the value *A/B* will correspond to the nonstoichiometric magnetite with the chemical formula:



On the other hand, it is useful to consider the surface effects. It has been reported that the magnetic moments of some iron cations in the NPs could be pinned when they belong to the surface layer, due to the presence of high magnetic anisotropy [46]. Consequently, not all *B*-site iron ions undergo electron hopping in response to the surface effects. In this case, we may try to evaluate some of the iron ions participating in the electron $Fe^{2+} \rightleftharpoons Fe^{3+}$ exchange in the stoichiometric magnetite at $T > T_V$. From the Mössbauer line intensities and hyperfine parameters, we derive the charge distribution, as follows:



From the above analysis of the core-shell structure, we find that the core region is a stoichiometric and has a major contribution for Verwey transition “ T_V ” in SD.

The quantitative size of the core-shell structure of SD is analyzed using Mössbauer spectroscopy based on the distribution of Fe^{3+} and Fe^{2+} cations at the *A* and *B* site and is found to be approximately 277@493 nm. Additionally, the observed magnetic moment “*M*” per formula unit for the stoichiometric core region of Fe_3O_4 is approximately $4.0\mu_B$ with density, $\rho \sim 5.1 \text{ g/cm}^3$, whereas the shell component (nonstoichiometric) has “*M*” $\sim 3.68\mu_B$ with $\delta = 0.074$ ($\rho \sim 4.66 \text{ g/cm}^3$) and is hence represented as $Fe_{2.93}O_4$. The calculated value of M_S based upon the Mössbauer analysis is approximately 87 emu/g, which is very close to 83 emu/g, as obtained from dc magnetic measurements. For NSD, it is clearly observed that the presence of three sextets: one for Fe^{3+} cations at the *A* site and two for Fe^{2+} , Fe^{3+} cations at the *B* site, as shown in Fig. 3(d). Here, the presence of two sextets at the *B* site, each from Fe^{3+} and Fe^{2+} cations, indicates clearly the absence of electron hopping ($Fe^{2+} \rightleftharpoons Fe^{3+}$) above T_V . Based upon a comparative analysis of magnetization data of bulk and the NSD sample, the observed magnetic moment “*M*” per formula unit for the nonstoichiometric disc is approximately $3.48\mu_B$ throughout the region and density “ ρ ” $\sim 4.43 \text{ g/cm}^3$ (as given in Table I).

It is anticipated that the ND system should have a vortex domain structure and should possess an onion structure under application of sufficiently high magnetic field [3,27]. Such a property has been further studied by micromagnetic simulation through Mumax3.9 software. The clear observation of core (vortex core) in the center of SD at $H=0$ and its gyrotropic movement under the application of external field, $H > 0$, provides evidences of a vortex configuration in SD. In such a magnetic vortex domain structure, the hysteresis loop is composed of a two-step magnetization reversal process, which involves onion-to-vortex transition and vice versa [47,48]. At large external magnetic field (*H*), SD falls into a saturation state or a single domain state, as shown in Fig. 3(a(ii)) because all spins are parallel to the field direction. The complete phenomena of hysteresis loop (vortex, onion, annihilation, and *c* state) in the SD nanomaterial is represented in Fig. 3(a(i–v)), where the green color indicates saturation magnetization in positive direction and navy color indicates the saturation moment in negative direction.

The negligible coercive field and remanence are expected to emerge in SD through simulation. Such a difference between experimental results and simulated envelope can be interpreted as an effect of the polydispersity of the sample, which is not taken into account in the magnetic hysteresis simulation. Several experimental studies of the magnetic vortex state in ferromagnetic nanodisks and nanodots have been performed using magnetic force microscopy [49,50], Lorentz microscopy [50,51], and magneto-optical techniques [52–54], which is in a good agreement with numerical micromagnetic simulation. Indeed, micromagnetic simulation is a robust numerical technique to probe the existence of vortex configuration and is therefore used to confirm the magnetic vortex configuration for the nanodisc samples. A micromagnetic phase diagram is constructed based upon the lower-energy state and the relative stability of magnetic phases as a function of diameter “*d*” and thickness “*t*” [Fig. 4(b)]. This phase diagram is based on the Landau-Lifshitz-Gilbert (LLG) equations (Appendix) and more detail about its construction is given the Appendix. It is clearly observed that the nanodisc samples are found in the vortex region and far from any limit of other possible ground state. We find the point at which the three ground states have the same energy, the so-called “triple point” (“*t*” $\sim 80 \text{ nm}$ and “*d*” $\sim 66 \text{ nm}$) and clearly separates the three-ground-state region, i.e., in-plane single

TABLE I. Quantitative analysis of physical, structural, and magnetic composition of SD and NSD based upon the core-shell model.

Sample code	Percentage (%) ($\pm 2\%$)	Size (nm) ($\pm 15 \text{ nm}$)	Magnetization, M_S (emu/g)	Magnetic moment (μ_B)	Density, ρ (g/cm^3)
SD	Core—36	Core—277	Core—92	Core—4.00	Core—5.10
	Shell—64	Shell—493	Shell—83	Shell—3.68	Shell—4.66
NSD	No core-shell	745	80	3.48	4.43

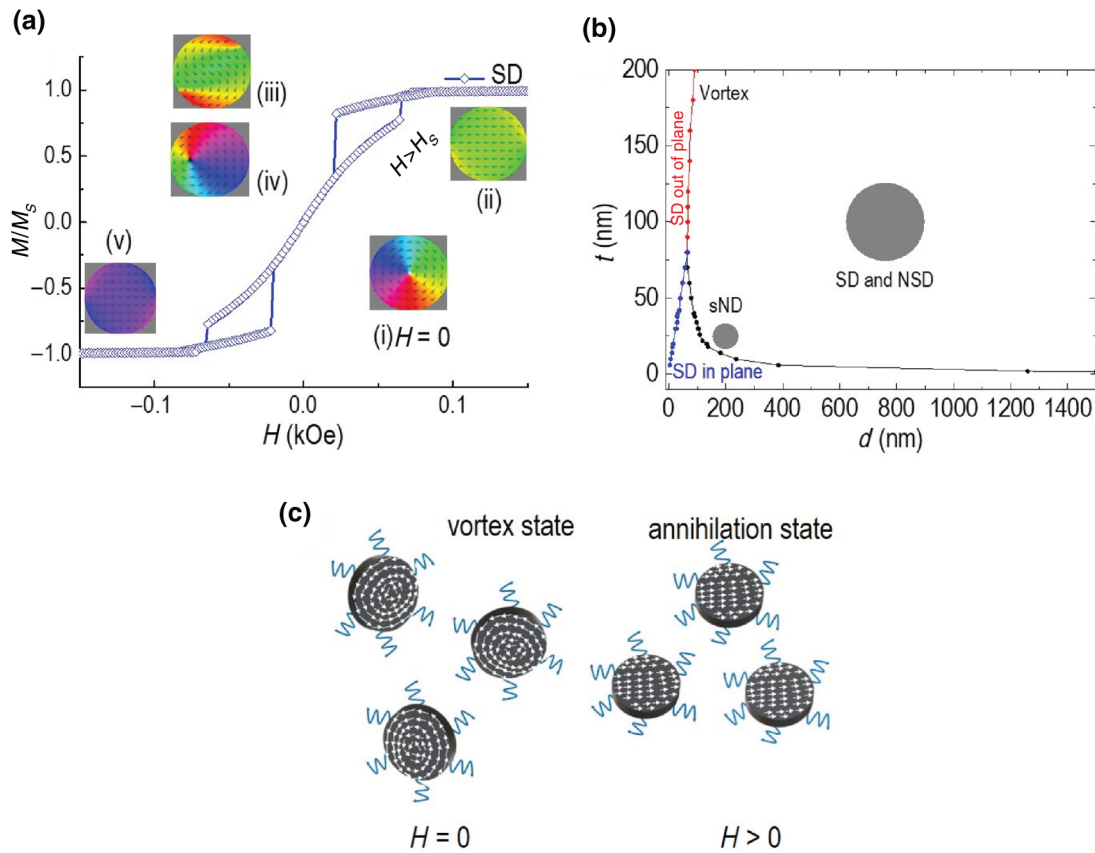


FIG. 4. (a) Simulated hysteresis loop showing magnetic states during switching of SD, (b) Represent the phase diagram of nanodiscs indicating the region of single-domain out-of-plane, single-domain in-plane, and vortex state as a function of thickness and diameter, (c) Schematic illustration of the vortex and onion state of SD in dispersion in the absence and presence of external magnetic field “ H ”, respectively. Arrows indicate the spin direction.

domain, out-of-plane single domain, and vortex region (multidomain). From the simulation, we find that the critical diameter (d_c) approximately 66 nm; below which the single domain region and above which the multidomain region occurs (single domain $< d_c <$ vortex or multidomain), is very close to the theoretical critical size (d_c) approximately 64 nm for Fe_3O_4 [22]. A detail analytical description to find the phase boundary between the in-plane, out-of-plane, and vortex magnetic phases is discussed in Refs. [52,55]. In this way, we construct and analyze the ground states in magnetic nanodiscs providing explicit transition lines between vortex and in-plane and out-of-plane single domain states, which is in a good agreement with Refs. [52,56–58] and hence provides explicitly the magnetic vortex configuration in the nanodisc samples.

The contribution of stoichiometric NDs on the heating profile versus the nonstoichiometric component is analyzed using calorimetric experiments. The samples are first coated with biocompatible citric acid as a stabilizer, Fig. S3 within the Supplemental Material [34]. The SAR values are evaluated based on the temperature

versus time curves. To analyze the heating efficiency, the samples are exposed to an ac magnetic field ($H = 200$ Oe, 300 Oe, and 450 Oe, $f = 107$ kHz) under biologically safe conditions; the maximum product of our condition is $H \times f = 3.8 \times 10^9 \text{ Am}^{-1} \text{ s}^{-1}$, which is under Dutz conditions ($5.1 \times 10^9 \text{ Am}^{-1} \text{ s}^{-1}$) [59]. It is observed that the heat generated after 5–6 min of application of magnetic field “ H ” and frequency “ f ” produce a small increase in temperature, ΔT , for the investigated samples (Fig. S5 within the Supplemental Material [34], which is expected for large ferrimagnetic NPs. Generally, the heating performance displayed by large NPs depends on the hysteresis loss, due to its size dependency along with applied field and frequency. Figure 5(a) shows the experimental and simulated SAR values for SD and NSD. The obtained SAR values are rather low, approximately 5 W/g for NSD, 6.5 W/g for SD, and approximately 7 W/g for SD (obtained through simulation). The SAR value of SD is slightly higher than NSD. However, it is worthwhile to remark that, quantitatively, the difference observed between experimental SAR values of SD and NSD are rather small, falling within the experimental errors. However, the heating

profile as supports our assumption of the different contribution in the SAR development brought by stoichiometric over nonstoichiometric Fe.

The discrepancy between experimental and simulated SAR values is probably due to the scattered alignment of nanodiscs, in accordance with the previous published data [3,60]. The obtained SAR values for SD and NSD systems are much smaller than those reported by Yang *et al.* [3] and Ma *et al.* [61]. Nevertheless, it should be noted that even though the SAR values reported by Yang *et al.* [3] are among the highest reported so far in the literature, these materials remain difficult to implement in real clinical trials, because the product of the field strength and frequency ($H \times f$) range from 7.8×10^9 to $2.3 \times 10^{10} \text{ A m}^{-1} \text{ s}^{-1}$ and exceed the upper safe limit of $5 \times 10^9 \text{ A m}^{-1} \text{ s}^{-1}$. Indeed, their SAR values will be lower under the application of magnetic fields that falls within the clinical relevant conditions.

For the field ($H = 400$ Oe, 600 Oe) below switching field “ H_S ”, no appreciable hysteresis loss is observed, which clearly indicates that the field amplitude is not sufficient to promote the nucleation of the vortex state to onion,

and hence results in a low SAR value. Due to the limitation of the experimental setup, the maximum field and frequency ($H = 450$ Oe; $f = 107$ kHz), further, we simulate the SAR values for SD obtained above the “ H_S ”. The field-dependence-simulated hysteresis curves at 400–800 Oe is shown in Fig. S6 within the Supplemental Material [34]. A significant hysteresis loss is observed at “ H ” = 800 Oe due to the switching phenomenon, which takes place around 600 Oe, thereafter vortex is nucleated to the onion state. Theoretically, area A of a particular hysteresis loop can be calculated in the variables (M/M_S , H). Hence the corresponding SAR value is then calculated by the following equation [22,62]

$$\text{SAR} = \frac{10^{-7} M_S f A}{\rho} \text{ W/g}, \quad (3)$$

where ρ is the nanoparticle density, i.e., for magnetite, $\rho = 5.1 \text{ g/cm}^3$. The inset in Fig. S6(a) within the Supplemental Material [34], represents the simulated SAR value at different field “ H ” and frequency “ f ” where an increase in SAR with “ H ” is observed at “ H ” = 600 Oe.

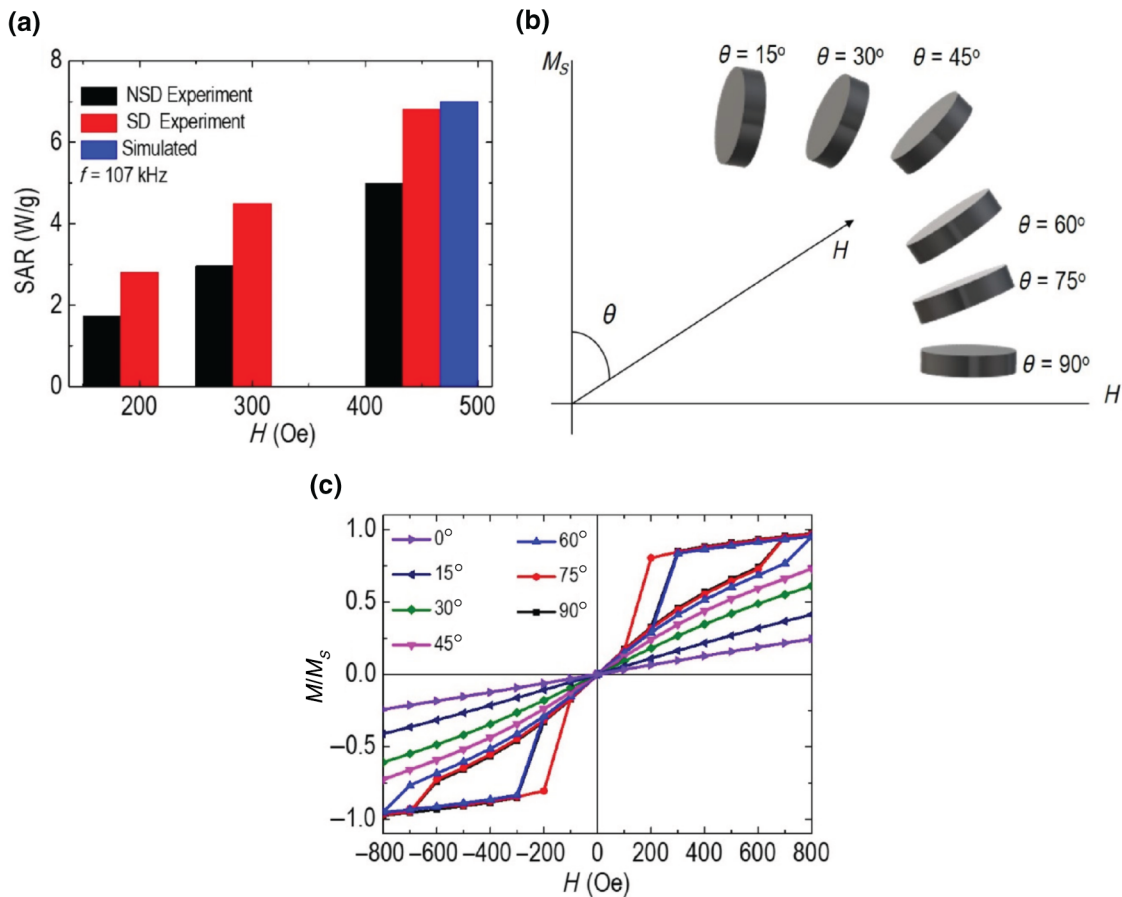


FIG. 5. (a) Experimental and simulated SAR value NSD and SD (error bars indicate the standard error of the means of different SAR measurements). (b) Orientation of NDs with the application of magnetic field at different angle (θ), and (c) represents the hysteresis loops of SD at different directions at “ H ” = 800 Oe.

At low field, the observed SAR has a rather small value (<50 W/g). When “ H ” is more than 600 Oe, the SAR rises sharply and reaches approximately 184 W/g (“ f ” = 107 kHz; “ H ” = 800 Oe). In fact, the simulated value of SAR for “ H ” in the range from 600–800 Oe, there is a rapid increase in its value due to the inset of switching field, see Fig. S6a within the Supplemental Material [34].

Recently, it is reported that the orientation-dependent hysteresis loop of NDs with respect to ac magnetic field has a significant impact in the enhancement of SAR value [3,18,24]. The inclination of each SD in the application of field “ H ” is shown schematically in Fig. 5(b), where symbol “ θ ” represents the angle between the magnetic field “ H ” and the normal direction of the SD. The hysteresis loops of SD along these incline directions are obtained through simulation, as shown in Fig. 5(c), which disclose the possible anisotropic magnetization reversal behaviors of circular SD [63].

For $\theta = 0^\circ$ – 45° , no hysteresis loss is observed. In the vicinity of the center of the nanodiscs, the angle between adjacent spins becomes increasingly large when the spin directions remain confined in plane. Consequently, at the core of the vortex structure, the magnetization within a small spot will turn out of plane and parallel to the plane normal. Although, the concept of such magnetic vortex with a turned-up magnetization core is introduced, direct experimental evidence for this phenomenon is still lacking. In the present work, the SD clearly shows the vortex core whose spin configuration will be out of plane under the application of field in perpendicular direction ($\theta = 0^\circ$), and hence will contribute nonzero magnetization [Fig. 4(a)]. This is in a good agreement with the study reported on the vortex state in magnetic nanodots and discs exhibiting a core region in which the magnetization has a nonzero component in the z axis, i.e., perpendicular direction [49,64,65]. From Fig. 5(c), no significant hysteresis loss is observed in out-of-plane magnetization ($\theta = 0^\circ$). The heating properties of nanodiscs depend on the area of hysteresis loss. Therefore, we believe that the present SD shows no significant heating efficiency in the perpendicular direction even at higher magnetic field [$H = 800, 3000$ Oe Figs. 5(a) and 5(b)].

The multiswitching in hysteresis loop is observed when θ lies between 60° – 90° . Figure 6(a) shows simulated direction-dependent SAR values of SD and it is clearly seen that the SAR changes efficiently with orientation. When $\theta = 60^\circ$, the SAR rises quickly and reaches a maximum value of approximately 270 W/g. The rapid increase in SAR at $\theta = 60^\circ$ can be ascribed to the occurrence of multiswitching hysteresis behavior at “ H_S ”~700 Oe, clearly observed in the inset of Fig. 6(a). When $\theta > 60^\circ$, the SAR value starts to decrease until $\theta = 90^\circ$, which indicates the stability of the vortex state for a longer time at $\theta = 60^\circ$, whereas the vortex state just undergoes a brief stay and is then swiftly annihilated at $\theta = 75^\circ$ and 90°

[63]. Thus, higher SAR is observed in the parallel alignment of SD at “ θ ” = 60° to 90° . The orientation of SDs for $\theta = 60^\circ$ to 90° at “ H ” = 800 Oe can be considered as a vortex region owing to their lowest total energy as shown in Fig. 7(a). It is generally believed that nanostructures with vortex domain structure should enhance the hysteresis loss due to existence of different switching field H_S but it does not mean that only the existence of vortex state is sufficient to enhance the hysteresis loss and hence the SAR value [3,18,27].

For this, the first requirement is the applied field “ H ” should be able to nucleate the vortex state to the onion state and this is possible only when $H > H_S$, where “ H_S ” depends on size and shape [66,67]. In order to further strengthen this point, we consider and simulate the small hypothetical NDs (as denoted here by SND) of diameter “ d ” = 200 nm and thickness “ t ” = 25 nm with aspect ratio “ β ” = t/d = 0.13 (same as for our SD) and exhibits the magnetic vortex configuration, shown in phase diagram Fig. 4(b). We perform direction-dependent hysteresis loss at similar simulation condition as for SD. The observed hysteresis losses are given in Fig. S6(b) within the Supplemental Material [34] consisting of switching field “ H_S ” approxiamtely 360 Oe (<for SD) and their respective SAR value is shown in Fig. 6(a). In comparison, the simulated result for SND and SD, the SAR value of SND is approximately 4 times higher than that of SD, i.e., 1028 W/g, which agrees well with the fact that the size is almost 4 times smaller than SD. However, the observed remanence magnetization is very high, which indicates the possibility aggregation in SND. Here, the higher SAR of SD is obtained at $\theta = 60^\circ$ whereas at $\theta = 90^\circ$ for SND. These results suggest that circular NDs provoke a higher SAR in parallel alignment, and should be in the range $\theta = 60^\circ$ – 90° for $H = 800$ Oe. In addition, the lowest total energy of SND is lies in these direction (particularly $\theta = 75^\circ$ – 90°), Fig. 7(b), similar to the SD as discussed above. Although the higher SAR of SD and SND are at different orientation (“ θ ”), interestingly the switching field “ H_S ” is well consistent with obtained SAR for both samples, i.e., higher SAR at higher “ H_S ” at a respective angle “ θ ” as shown in the inset of Fig. 6(a). These results indicate an interesting connection between the size, orientation, and switching field, which affect tuning the SAR value for circular Fe_3O_4 NDs.

Furthermore, we explore this correlation at higher field (“ H ” = 3000 Oe) by analyzing similar angle-dependent hysteresis loss. The obtained hysteresis loss is shown in Fig. S7 within the Supplemental Material [34] and its corresponding SAR values is in Fig. 6(b). At $\theta = 0^\circ$ and 5° , no hysteresis loss is observed and the multiswitching in hysteresis loss takes place at $\theta = 10^\circ$ – 90° . When $\theta = 15^\circ$, the SAR rises quickly and reaches a maximum value approximately 340 W/g and approximately 1452 W/g for SD and SND, respectively. The direction-dependent higher SAR

is obtained at $\theta = 15^\circ$, which contradicts with direction-dependent higher SAR at “ H ” = 800 Oe. This contradiction of angle-dependent SAR at different field is probably due to the connection between the switching field (size), orientation, and applied field during the formation of vortex in the SD and SND. In addition, there is always the possibility of anisotropic magnetization-reversal behaviors of NDs as mentioned above. However, the switching field “ H_S ” is still well consistent with the SAR value of SD and SND, i.e., higher SAR at higher switching field “ H_S ”, as shown in the inset of Fig. 5(b). In both cases (“ H ” = 800 Oe and “ H ” = 3000 Oe), the angle-dependent SAR is in complete agreement with “ H_S ” and hence a higher SAR is observed in higher “ H_S ” regardless of orientation and applied field.

Furthermore, to study the effect of geometrical parameters on switching field “ H_S ”, we analyze a thickness, i.e., “ t ” (25–300 nm) and a diameter, i.e., “ d ” (100–770 nm), dependent hysteresis loss in reference of SD, Fig. S6(c,d) within the Supplemental Material [34]. The observed “ H_S ” and SAR are shown in Figs. 6(c) and 6(d). The

obtained SAR values increase with diameter “ d ” and reach a maximum value of approximately 348 W/g at “ d ” = 600 nm [i.e., at higher “ H_S ” as shown in the inset of Fig. 6(d)], but starts to decrease to approximately 180 W/g at “ d ” = 770 nm at constant thickness “ t ” = 100 nm. The total energy (E_{tot}) decreases with increasing diameter “ d ” and reaches a minimum at “ d ” = 770 nm in our observation limit as clearly seen in Fig. 7(d). Owing to lower energy at “ d ” = 770 nm, one can expect higher SAR at “ d ” = 770 nm instead of at “ d ” = 600 nm. But this result is ascribed due to the stable vortex configuration at “ d ” = 600 nm as compared with “ d ” = 770 nm, which can efficiently enhance the hysteresis loss. This result indicates that although the vortex configuration is observed in SD, perfect geometry for its stability is a major factor to enhance the heating efficiency significantly, which is observed at “ d ” = 600 nm rather than at “ d ” = 770 nm in the present work. Thus, we anticipate the region of vortex configuration of SD is in the range of “ d ” = 600–770 nm at “ t ” = 100 nm, which is the most energetically preferred region as shown in Fig. 7(d) and lies within the vortex region given in the magnetic

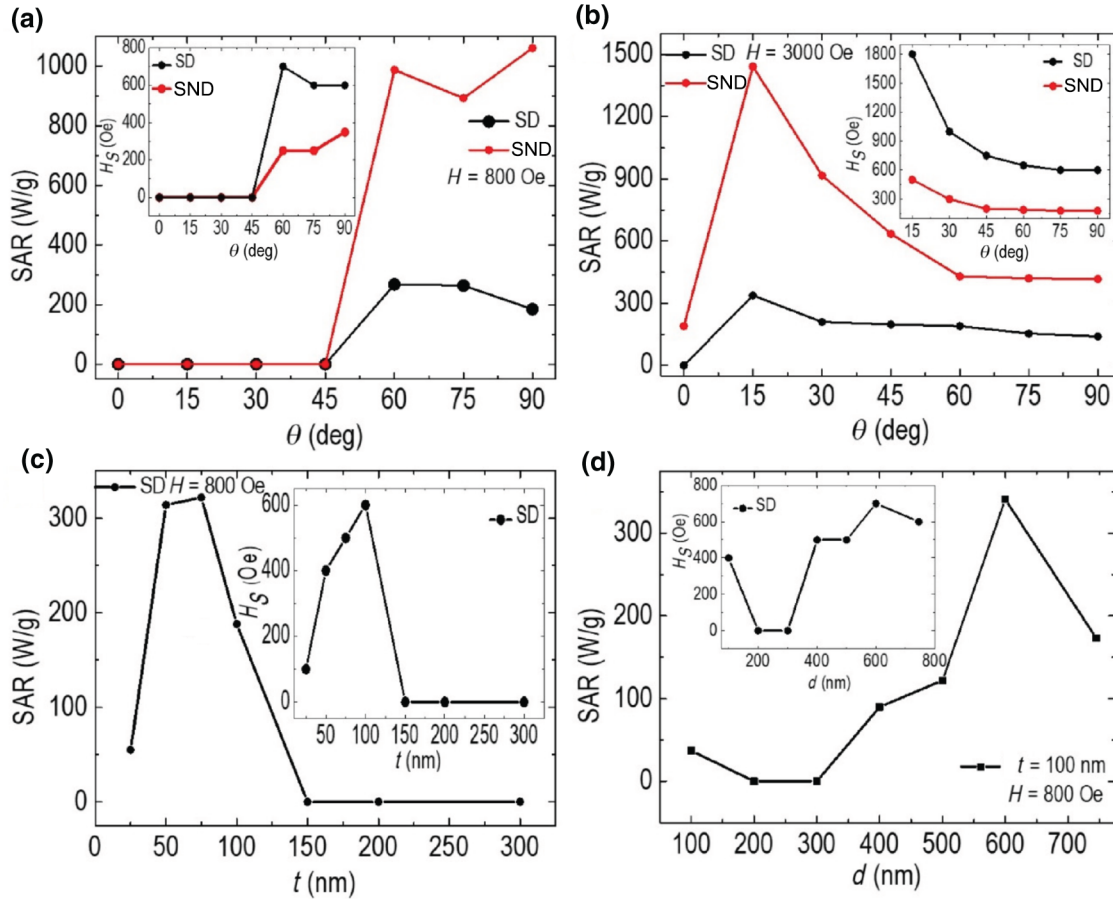


FIG. 6. (a), (b) Direction-dependent SAR value of SD and SND at $f = 107$ kHz and respective insets show an angle-dependent switching field “ H_S ”, respectively, and (c) and (d) thickness “ t ” and diameter “ d ”-dependent SAR value of SD at $f = 107$ kHz and respective insets show thickness “ t ” and diameter “ d ”-dependent switching field “ H_S ”, respectively.

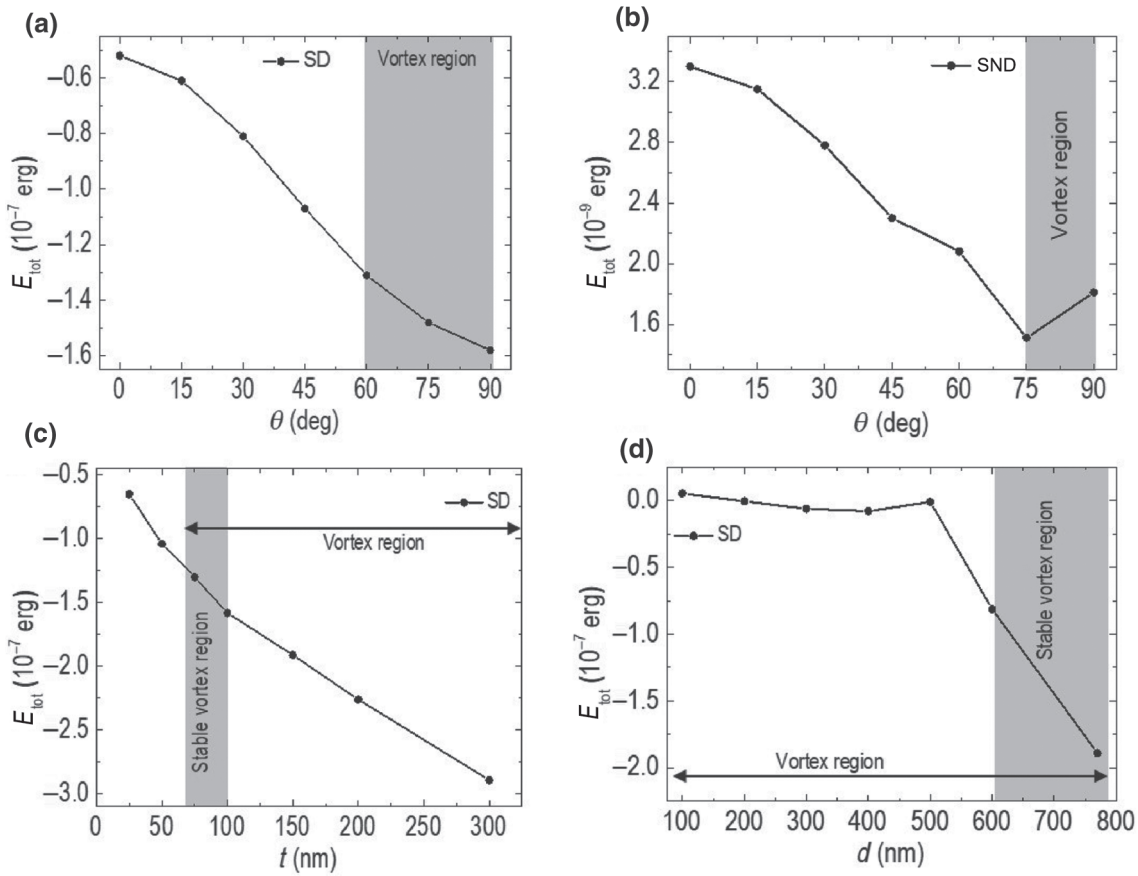


FIG. 7. (a), (b) Total energy (E_{tot}) of the SD and SND in application of field $H = 800$ Oe, and (c), (d) total energy (E_{tot}) of the SD with respect to thickness “ t ” and diameter “ d ” at $H = 800$ Oe.

phase diagram, Fig. 4(b). Here, whatever the vortex configuration, our concern is with diameter “ d ” dependent switching field and its effect on the SAR.

Thus the observed result of higher SAR at higher “ H_S ” further confirms the relation between switching field and SAR as shown in Fig 6(d). Similarly, the hysteresis loops for SD with thickness ranging from “ t ” = 25–300 nm at constant diameter 770 nm, the observed highest SAR is approximately 322 W/g at t = 75 nm, as shown in Fig. 6(c), and 188 W/g at t = 100 nm (“ H ” = 800 Oe and “ f ” = 107 kHz). Here, the highest SAR is observed at the second highest switching field “ H ” = 500 Oe, which is quite different than our expectation. This is probably due to the absence of perfectness of geometry for vortex configuration as mentioned above. Thus, the anticipated region “ t ” = 65–100 nm is the vortex-configuration region at “ d ” = 770 nm suggesting SD with “ t ” = 75 nm and “ d ” = 770 nm has most stable vortex configuration due to which higher heating efficiency is observed at higher switching field “ H_S ”. The corresponding total energy (E_{tot}) decreases with increasing thickness “ t ” and the corresponding vortex region, as shown in Fig. 7(c), is well agreed with magnetic phase diagram, Fig. 4(b). It can

be worthwhile to mention that SD seems to be flat with increasing diameter (decreasing thickness) at constant “ t ” (“ d ”), which means it grows towards thinner from thicker with small aspect ratio ($\beta = t/d$). For a thinner particle (“ t ” \ll “ d ”), the bending state tends to rotate as a whole with a decrease in the applied magnetic field. Therefore, the lowest energy state, i.e., the vortex configuration, is not accessible during evolution of the magnetization pattern in external magnetic field. At “ t ” = 25 nm, the vortex could not nucleate during magnetization reversal, probably due to the small thickness (“ t ” \ll “ d ”) of the SD where the magnetization reversal resembles the process of quasiuniform rotation. When the thickness of SD is above 100 nm, the SAR abruptly falls to zero due to the absence of hysteresis loss. Thus, the behavior of the particle resembles a single-domain one, although the actual particle size exceeds the effective single-domain regime. The shape of SD is grown towards tubular structure with the increase of thickness and one can expect the higher hysteresis loss owing to the contribution of shape anisotropy. However, the size of these tubular structure is larger for which “ H ” = 800 Oe is insufficient to generate the hysteresis and hence no efficient hysteresis loss is observed.

IV. CONCLUSION

In conclusion, we present a circular magnetic vortex NDs of Fe_3O_4 and investigate their heating properties by both experimental as well as theoretical simulations. It is observed that the heating performance is better for stoichiometry Fe_3O_4 nanodiscs as compared with the non-stoichiometry version owing to charge ordering between Fe^{2+} and Fe^{3+} , which is further tuned by controlling the switching field-mediated shape, size, and orientation of nanodiscs in the direction of applied field in a controlled way. The larger the switching field, the higher the observed SAR value. These findings could be a useful insurgency in magnetic vortex nanoparticles that the existence of vortex configuration is not only a factor to enhance heating capability but switching field mediated by shape, size, and orientation are also relevant factors to consider. Finally, this study sheds light onto the effective design of vortex-configuration Fe_3O_4 nanodiscs and studying their heating performance by systematically adjusting their size, shape, orientation-mediated switching field, and stoichiometry.

ACKNOWLEDGMENTS

G.N. is grateful to the Brazilian funding agency CAPES and PPGF-UFMA for providing doctorate fellowship and other financial support to visit UnB, Brasilia, CBPF, Rio de Janeiro to perform the experiment, respectively. We are grateful to Professor Dr Francisco Sinfronio for providing the facility to synthesize the materials using a commercial Synthwave microwave system. We are also grateful to Professor Stephen McVitie for helpful discussions. G.Z. thanks the support of the ERDF project “Development of pre-applied research in nanotechnology and biotechnology” (No. CZ.02.1.01/0.0/0.0/17_048/0007323)

APPENDIX

Micromagnetic simulation hysteresis loop for nanodiscs: the micromagnetic simulations are performed using the Mumax3.9 package. The dynamic response to fast external-field changes is considerably different from that described by the hysteresis loop, and is in general governed by the Landau-Lifshitz-Gilbert Langevin equation:

$$\frac{\partial M(r,t)}{\partial t} = \frac{-r}{1+\alpha^2} M(r,t) * H_{\text{eff}} - \frac{r\alpha}{(1+\alpha^2)M_S} M(r,t) * [M(r,t) * H_{\text{eff}}], \quad (\text{A1})$$

where

$$H_{\text{eff}} = \frac{\partial E_{\text{tot}}}{\partial M_S}. \quad (\text{A2})$$

Here, $M(r,t)$ is the magnetization distribution, H_{eff} is the effective field, M_S is the saturation magnetization, γ is the

gyromagnetic ratio ($1.78 \times 10^7 \text{ s}^{-1} \text{ Oe}^{-1}$). The total energy (E_{tot}) is the sum of five terms, namely exchange energy, self-magnetostatic energy, magnetocrystalline anisotropy energy, surface anisotropy energy, and Zeeman energy.

Law of saturation approach (LAS): we calculate the surface anisotropy by using the law of approach to magnetic saturation [42], expressed by the following equation:

$$M = M_S \left(1 - \frac{b}{H^2} \right), \quad (\text{A3})$$

where b is a factor correlated with the effect of the magnetocrystalline anisotropy. In the case of uniaxial magnetic crystals, the fitting parameter b can be used to obtain an estimate of the anisotropy term K :

$$K = \mu_0 M_S \left(\frac{15b}{4} \right)^{1/2}. \quad (\text{A4})$$

-
- [1] M.-T. Chang, L.-J. Chou, C.-H. Hsieh, Y.-L. Chueh, Z. L. Wang, Y. Murakami, and D. Shindo, Magnetic and electrical characterizations of half-metallic Fe_3O_4 nanowires, *Adv. Mater.* **19**, 2290 (2007).
 - [2] F. X. Redl, C. T. Black, G. C. Papaefthymiou, R. L. Sandstrom, M. Yin, H. Zeng, C. B. Murray, and S. P. O’Brien, Magnetic, electronic, and structural characterization of non-stoichiometric iron oxides at the nanoscale, *J. Am. Chem. Soc.* **126**, 14583 (2004).
 - [3] Y. Yang, X. Liu, Y. Lv, T. S. Herng, X. Xu, W. Xia, T. Zhang, J. Fang, W. Xiao, and J. Ding, Orientation mediated enhancement on magnetic hyperthermia of Fe_3O_4 nanodisc, *Adv. Funct. Mater.* **25**, 812 (2015).
 - [4] H.-M. Fan, J.-B. Yi, Y. Yang, K.-W. Kho, H.-R. Tan, Z.-X. Shen, J. Ding, X.-W. Sun, M. C. Olivo, and Y.-P. Feng, Single-crystalline MFe_2O_4 nanotubes/nanorings synthesized by thermal transformation process for biological applications, *ACS Nano* **3**, 2798 (2009).
 - [5] W. Wu, X. Xiao, S. Zhang, J. Zhou, L. Fan, F. Ren, and C. Jiang, Large-scale and controlled synthesis of iron oxide magnetic short nanotubes: Shape evolution, growth mechanism, and magnetic properties, *J. Phys. Chem. C* **114**, 16092 (2010).
 - [6] L. H. Reddy, J. L. Arias, J. Nicolas, and P. Couvreur, Magnetic nanoparticles: Design and characterization, toxicity and biocompatibility, pharmaceutical and biomedical applications, *Chem. Rev.* **112**, 5818 (2012).
 - [7] S. Dutz and R. Hergt, Magnetic particle hyperthermia - A promising tumour therapy?, *Nanotechnology* **25**, 452001 (2014).
 - [8] E. A. Pérgo, G. Hemery, O. Sandre, D. Ortega, E. Garaio, F. Plazaola, and F. J. Teran, Fundamentals and advances in magnetic hyperthermia, *Appl. Phys. Rev.* **2**, 041302 (2015).
 - [9] Z. Nemat, J. Alonso, L. M. Martinez, H. Khurshid, E. Garaio, J. A. Garcia, M. H. Phan, and H. Srikanth, Enhanced magnetic hyperthermia in iron oxide nano-octopods: Size and anisotropy effects, *J. Phys. Chem. C* **120**, 8370 (2016).

- [10] R. R. Shah, T. P. Davis, A. L. Glover, D. E. Nikles, and C. S. Brazel, Impact of magnetic field parameters and iron oxide nanoparticle properties on heat generation for use in magnetic hyperthermia, *J. Magn. Magn. Mater.* **387**, 96 (2015).
- [11] D. Ho, X. Sun, and S. Sun, Monodisperse magnetic nanoparticles for theranostic applications, *Acc. Chem. Res.* **44**, 875 (2011).
- [12] H. Khurshid, J. Alonso, Z. Nemati, M. H. Phan, P. Mukherjee, M. L. Fdez-Gubieda, J. M. Barandiarán, and H. Srikanth, Anisotropy effects in magnetic hyperthermia: A comparison between spherical and cubic exchange-coupled $\text{FeO}/\text{Fe}_3\text{O}_4$ nanoparticles, *J. Appl. Phys.* **117**, 17A337 (2015).
- [13] J. H. Lee, J. T. Jang, J. S. Choi, S. H. Moon, S. H. Noh, J. W. Kim, J. G. Kim, I. S. Kim, K. I. Park, and J. Cheon, Exchange-Coupled magnetic nanoparticles for efficient heat induction, *Nat. Nanotechnol.* **6**, 418 (2011).
- [14] A. H. Habib, C. L. Ondeck, P. Chaudhary, M. R. Bockstaller, and M. E. McHenry, Evaluation of iron-cobalt/ferrite core-shell nanoparticles for cancer thermotherapy, *J. Appl. Phys.* **103**, 07A307 (2008).
- [15] K. Simeonidis, C. Martinez-Boubeta, L. Balcells, C. Monty, G. Stavropoulos, M. Mitrakas, A. Matsakidou, G. Vourlias, and M. Angelakeris, Fe-Based nanoparticles as tunable magnetic particle hyperthermia agents, *J. Appl. Phys.* **114**, 103904 (2013).
- [16] R. Das, J. Alonso, Z. Nemati Porshokouh, V. Kalappattil, D. Torres, M. H. Phan, E. Garaio, JÁ García, J. L. Sanchez Llamazares, and H. Srikanth, Tunable high aspect ratio iron oxide nanorods for enhanced hyperthermia, *J. Phys. Chem. C* **120**, 10086 (2016).
- [17] D. F. Gutierrez-Guzman, L. I. Lizardi, J. A. Otálora, and P. Landeros, Hyperthermia in Low aspect-ratio magnetic nanotubes for biomedical applications, *Appl. Phys. Lett.* **110**, 133702 (2017).
- [18] X. L. Liu, Y. Yang, C. T. Ng, L. Y. Zhao, Y. Zhang, B. H. Bay, H. M. Fan, and J. Ding, Magnetic vortex nanorings: A new class of hyperthermia agent for highly efficient in vivo regression of tumors, *Adv. Mater.* **27**, 1939 (2015).
- [19] Z. Nemati, R. Das, J. Alonso, E. Clements, M. H. Phan, and H. Srikanth, Iron oxide nanospheres and nanocubes for magnetic hyperthermia therapy: A comparative study, *J. Electron. Mater.* **46**, 3764 (2017).
- [20] A. Muela, D. Muñoz, R. Martín-Rodríguez, I. Orue, E. Garaio, A. Abad Díaz De Cerio, J. Alonso, JÁ García, and M. L. Fdez-Gubieda, Optimal parameters for hyperthermia treatment using biominerallized magnetite nanoparticles: Theoretical and experimental approach, *J. Phys. Chem. C* **120**, 24437 (2016).
- [21] W. Zhang, X. Zuo, Y. Niu, C. Wu, S. Wang, S. Guan, and S. R. P. Silva, Novel nanoparticles with Cr^{3+} substituted ferrite for self-regulating temperature hyperthermia, *Nanoscale* **9**, 13929 (2017).
- [22] N. A. Usov, M. S. Nesmeyanov, and V. P. Tarasov, Magnetic vortices as efficient nano heaters in magnetic nanoparticle hyperthermia, *Sci. Rep.* **8**, 1224 (2018).
- [23] C.-J. Jia, L.-D. Sun, F. Luo, X.-D. Han, L. J. Heyderman, Z.-G. Yan, C.-H. Yan, K. Zheng, Z. Zhang, M. Takano, N. Hayashi, M. Eltschka, M. Kläui, U. Rüdiger, T. Kasama, L. Cervera-Gontard, R. E. Dunin-Borkowski, G. Tzvetkov, and J. Raabe, Large-Scale synthesis of single-crystalline iron oxide magnetic nanorings, *J. Am. Chem. Soc.* **130**, 16968 (2008).
- [24] D.-H. Kim, E. A. Rozhkova, I. V. Ulasov, S. D. Bader, T. Rajh, M. S. Lesniak, and V. Novosad, Biofunctionalized magnetic-vortex microdisks for targeted cancer-cell destruction, *Nat. Mater.* **9**, 165 (2010).
- [25] Y. Yang, X. L. Liu, J. B. Yi, Y. Yang, H. M. Fan, and J. Ding, Stable vortex magnetite nanorings colloid: Micro-magnetic simulation and experimental demonstration, *J. Appl. Phys.* **111**, 044303 (2012).
- [26] C. S. B. Dias, T. D. M. Hanchuk, H. Wender, W. T. Shigeyosi, J. Kobarg, A. L. Rossi, M. N. Tanaka, M. B. Cardoso, and F. Garcia, Shape tailored magnetic nanorings for intracellular hyperthermia cancer therapy, *Sci. Rep.* **7**, 14843 (2017).
- [27] R. Ferrero, A. Manzin, G. Barrera, F. Celegato, M. Coisson, and P. Tiberto, Influence of Shape, Size and magnetostatic interactions on the hyperthermia properties of permalloy nanostructures, *Sci. Rep.* **9**, 6591 (2019).
- [28] M. N. Nadagouda, T. F. Speth, and R. S. Varma, Microwave-Assisted green synthesis of silver nanostructures, *Acc. Chem. Res.* **44**, 469 (2011).
- [29] X. Hu, J. C. Yu, J. Gong, Q. Li, and G. Li, $\alpha - \text{Fe}_2\text{O}_3$ nanorings prepared by a microwave-assisted hydrothermal process and their sensing properties, *Adv. Mater.* **19**, 2324 (2007).
- [30] I. Bilecka and M. Niederberger, Microwave chemistry for inorganic nanomaterials synthesis, *Nanoscale* **2**, 1358 (2010).
- [31] C. A. F. Vaz, C. Athanasiou, J. A. C. Bland, and G. Rowlands, Energetics of magnetic ring and disk elements: Uniform versus vortex state, *Phys. Rev. B - Condens. Matter Mater. Phys.* **73**, 054411 (2006).
- [32] Y.-L. Chueh, M.-W. Lai, J.-Q. Liang, L.-J. Chou, and Z. L. Wang, Systematic study of the growth of aligned arrays of $\alpha - \text{Fe}_2\text{O}_3$ and Fe_3O_4 nanowires by a vapor-solid process, *Adv. Funct. Mater.* **16**, 2243 (2006).
- [33] S. Zhang, W. Wu, X. Xiao, J. Zhou, F. Ren, and C. Jiang, Preparation and characterization of spindle-like Fe_3O_4 mesoporous nanoparticles, *Nanoscale Res. Lett.* **6**, 1 (2011).
- [34] See Supplemental Material at <http://link.aps.org/supplemental/10.1103/PhysRevApplied.15.014056> for XRD, SEM images, FTIR, Mössbauer hyperfine parameters, Heating profiles, Field, direction, thickness and diameter dependent hysteresis loops.
- [35] B. D. Cullity and C. D. Graham, *Introduction to Magnetic Materials -Chapter 6 FERRIMAGNETISM* (Wiley Online Library, 2009), p.175.
- [36] E. P. Valstyn, J. P. Hanton, and A. H. Morrish, Ferromagnetic resonance of single-domain particles, *Phys. Rev.* **128**, 2078 (1962).
- [37] G. Salazar-Alvarez, J. Qin, V. Šepelák, I. Bergmann, M. Vasilakaki, K. N. Trohidou, J. D. Ardisson, W. A. A. Macedo, M. Mikhaylova, M. Muhammed, M. D. Baró, and J. Nogués, Cubic versus spherical magnetic nanoparticles: The role of surface anisotropy, *J. Am. Chem. Soc.* **130**, 13234 (2008).

- [38] D. J. Dunlop, Coercive forces and coercivity spectra of submicron magnetites, *Earth Planet. Sci. Lett.* **78**, 288 (1986).
- [39] F. Stacey and K. Wise, Crystal dislocations and coercivity in fine grained magnetite, *Aust. J. Phys.* **20**, 507 (1967).
- [40] F. Heider, D. J. Dunlop, and N. Sugiura, Magnetic properties of hydrothermally recrystallized magnetite crystals, *Science (80-.)* **236**, 1287 (1987).
- [41] W. S. Chiu, S. Radiman, R. Abd-Shukor, M. H. Abdullah, and P. S. Khiew, Tunable coercivity of CoFe_2O_4 nanoparticles via thermal annealing treatment, *J. Alloys Compd.* **459**, 291 (2008).
- [42] W. F. Brown, Theory of the approach to magnetic saturation, *Phys. Rev.* **58**, 736 (1940).
- [43] E. J. W. Verwey, Electronic conduction of magnetite (Fe_3O_4) and Its transition point at low temperatures, *Nature* **144**, 327 (1939).
- [44] J. P. Shepherd, J. W. Koenitzer, R. Aragn, J. Spalek, and J. M. Honig, Heat capacity and entropy of nonstoichiometric magnetite $\text{Fe}_{3(1-\delta)}\text{O}_4$: The thermodynamic nature of the verwey transition, *Phys. Rev. B* **43**, 8461 (1991).
- [45] T. Kim, S. Lim, J. Hong, S. G. Kwon, J. Okamoto, Z. Y. Chen, J. Jeong, S. Kang, J. C. Leiner, J. T. Lim, C. S. Kim, D. J. Huang, T. Hyeon, S. Lee, and J. G. Park, Giant thermal hysteresis in verwey transition of single domain Fe_3O_4 nanoparticles, *Sci. Rep.* **8**, 5092 (2018).
- [46] I. S. Lyubutin, C. R. Lin, Y. V. Korzhetskiy, T. V. Dmitrieva, and R. K. Chiang, Mössbauer spectroscopy and magnetic properties of hematite/magnetite nanocomposites, *J. Appl. Phys.* **106** (2009).
- [47] O. Kazakova, M. Hanson, A. M. Blixt, and B. Hjörvarsson, Domain structure of circular and ring magnets, *J. Magn. Magn. Mater.* **258**, 348 (2003).
- [48] A. Subramani, D. Geerpuram, A. Domanowski, V. Baskaran, and V. Metlushko, Vortex state in magnetic rings, *Phys. C Supercond.* **404**, 241 (2004).
- [49] T. Shinjo, T. Okuno, R. Hassdorf, K. Shigeto, and T. Ono, Magnetic vortex core observation in circular dots of permalloy, *Science (80-.)* **289**, 930 (2000).
- [50] J. Raabe, R. Pulwey, R. Sattler, T. Schweinböck, J. Zweck, and D. Weiss, Magnetization pattern of ferromagnetic nanodisks, *J. Appl. Phys.* **88**, 4437 (2000).
- [51] M. Schneider, H. Hoffmann, and J. Zweck, Lorentz microscopy of circular ferromagnetic permalloy nanodisks, *Appl. Phys. Lett.* **77**, 2909 (2000).
- [52] C. A. Ross, M. Hwang, M. Shima, J. Y. Cheng, M. Farhoud, T. A. Savas, H. I. Smith, W. Schwarzacher, F. M. Ross, M. Redjdal, and F. B. Humphrey, Micromagnetic behavior of electrodeposited cylinder arrays, *Phys. Rev. B - Condens. Matter Mater. Phys.* **65**, 1 (2002).
- [53] V. Novosad, K. Y. Guslienko, H. Shima, Y. Otani, S. G. Kim, K. Fukamichi, N. Kikuchi, O. Kitakami, and Y. Shimada, Effect of interdot magnetostatic interaction on magnetization reversal in circular Dot arrays, *Phys. Rev. B - Condens. Matter Mater. Phys.* **65**, 1 (2002).
- [54] R. P. Cowburn, D. K. Koltsov, A. O. Adeyeye, M. E. Welland, and D. M. Tricker, Single-Domain Circular Nanomagnets, *Phys. Rev. Lett.* **83**, 1042 (1999).
- [55] A. Aharoni, *Introduction to the Theory of Ferromagnetism* (Oxford University Press, Oxford, New York, 1996).
- [56] J. d'Albuquerque e Castro, D. Altbir, J. C. Retamal, and P. Vargas, Scaling Approach to the Magnetic Phase Diagram of Nanosized Systems, *Phys. Rev. Lett.* **88**, 2372021 (2002).
- [57] F. Poratti and M. Huth, Diagram of the states in arrays of iron nanocylinders, *Appl. Phys. Lett.* **85**, 3157 (2004).
- [58] K. L. Metlov and K. Y. Guslienko, Stability of magnetic vortex in soft magnetic nano-sized circular cylinder, *J. Magn. Magn. Mater.* **242–245**, 1015 (2001).
- [59] S. Dutz and R. Hergt, Magnetic nanoparticle heating and heat transfer on a microscale: Basic principles, realities and physical limitations of hyperthermia for tumour therapy, *Int. J. Hyperth.* **29**, 790 (2013).
- [60] H. Mamiya and B. Jeyadevan, Hyperthermic effects of dissipative structures of magnetic nanoparticles in large alternating magnetic fields, *Sci. Rep.* **1** (2011).
- [61] M. Ma, Y. Zhang, Z. Guo, and N. Gu, Facile synthesis of ultrathin magnetic iron oxide nanoplates by schikorr reaction, *Nanoscale Res. Lett.* **8**, 16 (2013).
- [62] J. Carrey, B. Mehdaoui, and M. Respaud, Simple models for dynamic hysteresis loop calculations of magnetic single-domain nanoparticles: Application to magnetic hyperthermia optimization, *J. Appl. Phys.* **109**, 083921 (2011).
- [63] H. Gao, T. Zhang, Y. Zhang, Y. Chen, B. Liu, J. Wu, X. Liu, Y. Li, M. Peng, Y. Zhang, G. Xie, F. Zhao, and H. M. Fan, Ellipsoidal magnetite nanoparticles: A New member of the magnetic-vortex nanoparticles family for efficient magnetic hyperthermia, *J. Mater. Chem. B* **8**, 515 (2020).
- [64] P. O. Jubert and R. Allenspach, Analytical approach to the single-domain-to-vortex transition in small magnetic disks, *Phys. Rev. B - Condens. Matter Mater. Phys.* **70**, 144402 (2004).
- [65] P. Landeros, J. Escrig, D. Altbir, D. Laroze, J. D'Albuquerque, E. Castro, and P. Vargas, Scaling relations for magnetic nanoparticles, *Phys. Rev. B - Condens. Matter Mater. Phys.* **71**, 094435 (2005).
- [66] K. Y. Guslienko, V. Novosad, Y. Otani, H. Shima, and K. Fukamichi, Magnetization reversal due to vortex nucleation, displacement, and annihilation in submicron ferromagnetic Dot arrays, *Phys. Rev. B - Condens. Matter Mater. Phys.* **65**, 244141 (2002).
- [67] A. Halder and A. O. Adeyeye, Vortex chirality control in circular disks using dipole-coupled nanomagnets, *Appl. Phys. Lett.* **106**, 032404 (2015).